

## Effect of ambient pressure on liquid swirl injector flow dynamics

Xiaodong Chen and Vigor Yang<sup>a)</sup>

*School of Aerospace Engineering, Georgia Institute of Technology, Atlanta, Georgia 30332-0150, USA*

(Received 18 August 2014; accepted 13 October 2014; published online 30 October 2014)

In this paper, a combined theoretical and numerical analysis is performed to study the internal and external flowfields of a liquid swirl injector. The effect of ambient pressure on the injector dynamics is explored systematically over a range of 1–50 atm. An increase in the ambient pressure increases the liquid film thickness, but decreases the spreading angle. This phenomenon can be attributed to the modification of the velocity profiles within the liquid film near the gas-liquid interface due to the alteration of the gas-phase shear stresses with pressure. The friction force at the interface plays a minor role. The generation and existence of stationary waves in the injector nozzle is also considered. At a higher ambient pressure, the pressure drop across the liquid sheet downstream of the injector exit increases, thereby suppressing the spreading of the liquid sheet. This in turn increases the thickness of the liquid sheet, and subsequently increases the breakup length at higher pressure. A semi-empirical model is developed to relate the velocity and pressure distributions near the surface of the liquid sheet. Good agreement is achieved between the measured and predicted shape and spreading angle of the liquid sheet. © 2014 AIP Publishing LLC. [<http://dx.doi.org/10.1063/1.4899261>]

### I. INTRODUCTION

This paper focuses on the effect of ambient pressure on the flow dynamics of a liquid swirl injector, as shown schematically in Fig. 1. It represents a generic configuration of many practical swirl injectors.<sup>1–3</sup> Liquid fluid is tangentially introduced into the vortex chamber and then centrifugal force causes it to form a swirling film attached to the wall. A hollow gas core exists in the center region to satisfy the conservation of angular momentum of the injected liquid. The liquid film exits the injector as a thin sheet and subsequently atomizes into a spray of droplets in the ambient gas. The atomization process involves two primary mechanisms: disintegration of the liquid sheet as it swirls, and sheet breakup into ligaments and then droplets.<sup>4</sup>

In classic hydrodynamic theories based on inviscid, incompressible flow assumptions,<sup>2</sup> the injector characteristics in terms of the exit film thickness and spreading angle are solely determined by a non-dimensional geometrical characteristic parameter  $A$ , defined by  $A = A_n R_{in} / A_{in} R_n$ , where  $R_n$  is the nozzle radius,  $R_{in}$  the radial location of the center of the inlet passage,  $A_n$  the nozzle area, and  $A_{in}$  the total area of the inlet passages. In practice, the injector characteristics are also influenced by the ambient flow conditions, although their specific effects on the injector flow dynamics are yet to be fully explored.

De Corso and Kemeny<sup>5</sup> conducted a pioneering study on the effect of ambient gas pressure on the spray behavior of a centrifugal nozzle with diesel fuel. The pressure drop across the fuel inlet varied from 0.17 to 2.7 MPa, and the ambient gas pressure covered a range of 0.01–0.8 MPa. The spray distribution was obtained by 28 radial sampling tubes spaced 5° apart on an arc of a circle of 114.3 mm radius centered at the nozzle exit. The nozzle diameter is not given, but was estimated

<sup>a)</sup> Author to whom correspondence should be addressed. Electronic mail: [vigor.yang@aerospace.gatech.edu](mailto:vigor.yang@aerospace.gatech.edu).

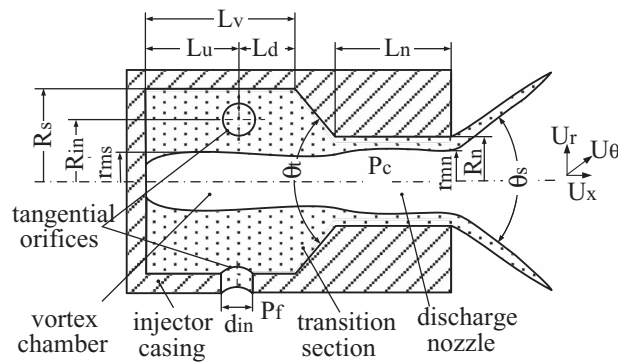


FIG. 1. Schematic of liquid swirl injector.

to be 3 mm from the experimental images. For a given pressure drop across the fuel injection orifice, the spray angle decreased markedly with increasing ambient pressure, and the shape of the spray changed from a cone to a bell. Measurements were made of the mean pressure at 12.7 mm downstream of the nozzle exit on the centerline. A clear decrease of the gas static pressure from its ambient value was observed. The phenomenon became even more obvious with increasing ambient pressure; the pressure difference across the fuel spray increased from 0.013 MPa for an ambient pressure of 0.01 MPa, to 0.15 MPa for an ambient pressure of 0.8 MPa. A generic hypothesis on the underlying mechanisms was suggested based on the aerodynamic effects on the spray.

Kim *et al.*<sup>6</sup> examined the spray characteristics of a water swirl injector in nitrogen by measuring the spreading angle of the liquid sheet before and after its breakup at various flow rates. The ambient nitrogen pressures covered a range of 0.1–4.0 MPa. The pressure drop across the water injection orifice varied from 0.061 to 0.579 MPa, which corresponded to a mass flow rate of 9–26 g/s. The liquid axial velocity in the nozzle was predicted to be 8.25–25.4 m/s, according to classic hydrodynamics theories.<sup>2</sup> At a fixed mass flow rate, the measured spreading angle of the liquid sheet prior to breakup remained almost independent of the ambient pressure. The liquid spray angle after the sheet breakup, however, was found to decrease with increasing ambient pressure. Two empirical correlations of the spreading angles before and after the sheet breakup were made, in terms of the gas/liquid density ratio and the Weber number based on the liquid film at the nozzle exit.

Kenny *et al.*<sup>7</sup> examined the effect of ambient pressure on the flow dynamics of a water swirl injector in air over a range of 0.10–4.83 MPa. The mass flow rate remained fixed at 90 g/s, and the axial velocity in the nozzle was about 50 m/s. An acrylic nozzle extension with a length of 14.35 mm was employed to provide optical access to the swirling flow development. Shadowgraphs of the liquid motion in the nozzle extension and near the exit were obtained. The internal film thickness increased with increasing ambient pressure. The phenomenon was attributed to the enhanced momentum loss at the gas/liquid interface at high pressures. The film thickness at the nozzle exit, however, was found to be insensitive to the ambient pressure within experimental uncertainties. Spatially stationary waves of the water flow were found to be present along the nozzle length, similar to the observation made by Hutt.<sup>8</sup> In contrast to the results of Kim *et al.*,<sup>6</sup> it was observed that the spreading angle of the liquid sheet decreased markedly with increasing ambient pressure. A relationship was established between the internal film thickness and the spreading angle of the liquid sheet at the nozzle exit. Since the exit film thickness was found to be insensitive to the ambient pressure, however, the conclusion that the internal film thickness played a significant role in determining the spray angle needs to be further clarified.

Much useful information has been obtained about the effect of ambient pressure on the film thickness and spray characteristics of swirl injectors, but limited by measurement capabilities, existing studies attempt to explain observed phenomena through assumed mechanisms, without exploring the underlying physics. In addition, conclusions on the spray angle are contradictory. For example, Kim *et al.*<sup>6</sup> observed that the spreading angle of the liquid sheet was almost constant,

while Kenny *et al.*<sup>7</sup> found that it decreased with ambient pressure. Both De Corso and Kemeny<sup>5</sup> and Kenny *et al.*<sup>7</sup> indicated a pressure difference across the liquid sheet issued from a swirl injector. The spreading angle measured by Kenny *et al.*,<sup>7</sup> however, showed good agreement with predictions without taking into account the pressure difference.

The present work attempts to clarify the unresolved issues surrounding the effects of ambient pressure on injector dynamics. An integrated theoretical and numerical model is established to investigate the effect of ambient pressure on the flow dynamics within and downstream of a liquid swirl injector. Several underlying mechanics and key parameters that dictate the injector characteristics are identified and systematically explored.

## II. THEORETICAL ANALYSIS

### A. Effect of viscous friction

Classical hydrodynamics theories for liquid swirl injectors were established based on the assumption of inviscid, incompressible flows. The spreading angle and thickness of the liquid sheet at the nozzle exit were found to be a sole function of a non-dimensional geometrical characteristic parameter  $A$ , independent of the ambient pressure.<sup>2</sup> In reality, viscous friction occurs along the chamber wall and at the liquid/gas interface. Existing theories only consider either the loss across the tangential inlet orifice<sup>2</sup> or the loss at the headend and in the transition section of the injector.<sup>9</sup> An improved theory should take into account all the mechanisms, so that the influence of ambient pressure on the injector flow behaviors can be properly considered.

Following the general analysis described in Ref. 2, the viscous effect can be properly treated by introducing the pressure and angular-momentum loss coefficients. The Bernoulli equation near the nozzle exit can be written as

$$P_f = P_c + \frac{\rho_l U_{\theta n}^2}{2} + \frac{\rho_l U_{xn}^2}{2} + \xi_{in} \frac{\rho_l U_{in}^2}{2} + \xi_v \frac{\rho_l U_{\Sigma}^2}{2} + \xi_n \frac{\rho_l U_{\Sigma}^2}{2}, \quad (1)$$

where the subscripts  $v$  and  $n$  denote the vortex chamber and discharge nozzle, respectively.  $P_f$  is the pressure in the liquid feed system at the tangential entry,  $P_c$  the ambient pressure,  $\rho_l$  the density of liquid,  $U_{\theta n}$  and  $U_{xn}$  the liquid tangential and axial velocity in the discharge nozzle, respectively,  $U_{in}$  the liquid velocity at the tangential entry, and  $U_{\Sigma}$  the total liquid velocity. The pressure loss coefficients of the tangential inlet, vortex chamber, and discharge nozzle are denoted by  $\xi_{in}$ ,  $\xi_v$ , and  $\xi_n$ , respectively. The loss of angular momentum can be introduced into the expression of  $U_{\theta n}$  as follows:

$$U_{\theta n} = \frac{K R_{in} U_{in}}{r_{mn}}, \quad (2)$$

where  $K$  is the angular-momentum loss coefficient,  $R_{in}$  the radial location of the center of the inlet passage, and  $r_{mn}$  the radius of the liquid film in the nozzle. The inlet velocity is determined by the mass continuity

$$U_{in} = \frac{\dot{m}_i}{n\pi r_{in}^2 \rho_l}, \quad (3)$$

where  $\dot{m}_i$  is the liquid mass flow rate, and  $n$  and  $r_{in}$  the number and radius of the inlet orifice, respectively.

The total mass flow rate through the injector nozzle can be represented as

$$\dot{m}_i = \varphi \pi R_n^2 \rho_l U_{xn} = \varphi \pi R_n^2 \sqrt{2\rho_l \Delta P_i - \rho_l^2 U_{\theta n}^2 - \xi_i \rho_l^2 U_{in}^2 - \xi_v \rho_l^2 U_{\Sigma}^2 - \xi_n \rho_l^2 U_{\Sigma}^2}, \quad (4)$$

where  $\varphi$  is the coefficient of passage fullness (i.e.,  $\varphi = 1 - r_{mn}^2/R_n^2$ ), and  $\Delta P_i = P_f - P_c$  is the pressure drop across the injector. The total velocity of liquid can be determined in terms of the pressure drop based on the Bernoulli equation

$$U_{\Sigma} = \sqrt{2\Delta P_i/\rho_l}. \quad (5)$$

By substituting the expression of the geometrical characteristic parameter  $A$ , the mass flow coefficient  $\mu_i$  can be obtained as follows:

$$\mu_i = \frac{\dot{m}_i}{\pi R_n^2 \sqrt{2\rho_l \Delta P_i}} = \sqrt{\frac{1 - \xi_v - \xi_n}{\frac{1}{\varphi^2} + \frac{A^2 K^2}{1-\varphi} + \xi_{in} \frac{A^2 R_n^2}{R_{in}^2}}}. \quad (6)$$

The film thickness inside the nozzle,  $h_i = (1 - \sqrt{1 - \varphi_i})R_n$ , can be obtained by solving the following relationship between  $\mu_i$  and the coefficient of passage fullness,  $\varphi_i$ :

$$\mu_i = \varphi_i \sqrt{\frac{\varphi_i}{2 - \varphi_i}}. \quad (7)$$

The spreading angle of the liquid film at the nozzle exit,  $\alpha$ , is determined from the ratio of the tangential to the total velocity

$$\sin \alpha = U_{\theta n} / U_{\Sigma n}, \quad (8)$$

where

$$U_{\theta n} = \frac{R_n}{r_{mn}} \mu_i A K \sqrt{\frac{2}{\rho_l} \Delta P_i}, \quad (9)$$

$$U_{\Sigma n} = \sqrt{U_{\theta}^2 + U_x^2 - \xi_{in} U_{in}^2 - \xi_v U_{\Sigma}^2 - \xi_n U_{\Sigma}^2} = \sqrt{1 - \xi_{in} \frac{A^2 R_n^2}{R_{in}^2} - \xi_v - \xi_n} \sqrt{\frac{2}{\rho_l} \Delta P_i}. \quad (10)$$

After some straightforward manipulations, we have

$$\sin \alpha = \frac{R_n}{r_{mn}} \frac{\mu_i A K}{\sqrt{1 - \xi_{in} \frac{A^2 R_n^2}{R_{in}^2} - \xi_v - \xi_n}}. \quad (11)$$

The pressure and angular-momentum loss coefficients are yet to be decided. The inlet loss  $\xi_{in}$  consists of two parts<sup>2</sup>

$$\xi_{in} = \xi_{inv} + \xi_{inf}, \quad (12)$$

where  $\xi_{inv}$  accounts for energy losses associated with vortices when the flow expands after the contraction near the inlet of the tangential orifice, and  $\xi_{inf}$  is the friction loss along the passage wall of the tangential orifice, which can be expressed as

$$\xi_{inf} = \lambda_{in} \frac{l_{in}}{d_{in}}. \quad (13)$$

The friction coefficient is  $\lambda_{in} = 0.3164/(\text{Re}_{in})^{1/4}$  for hydraulically smooth passages in the turbulent regime ( $\text{Re}_{in} > 4 \times 10^3$ ). The Reynolds number  $\text{Re}_{in}$  is defined as

$$\text{Re}_{in} = \rho_l U_{in} r_{in} 2\sqrt{n} / \mu_l = 2\dot{m}_i / (\pi \sqrt{n} r_{in} \mu_l), \quad (14)$$

where  $\mu_l$  is the liquid viscosity. The loss coefficients in the vortex chamber and discharge nozzle,  $\xi_v$  and  $\xi_n$  contain contributions from the frictions on the wall and along the liquid surface. Thus,

$$\xi_v = (\lambda_{wv} + \alpha \lambda_{gv}) \frac{L_v}{2R_v}, \quad (15)$$

$$\xi_n = (\lambda_{wn} + \alpha \lambda_{gn}) \frac{L_n}{2R_n}, \quad (16)$$

where  $\alpha$  is the gas-liquid density ratio, defined as  $\alpha = \rho_g / \rho_l$ . The subscript  $w$  and  $g$  denote the wall and liquid/gas interface, respectively. The friction coefficient for the wall is  $\lambda_{w(v,n)} = 0.3164 \text{Re}_{l(v,n)}^{-1/4}$ , where  $\text{Re}_{l(v,n)} = 2\rho_l U_{\Sigma} R_{(v,n)} / \mu_l$ . The subscripts,  $(v, n)$ , stand for the vortex chamber and discharge

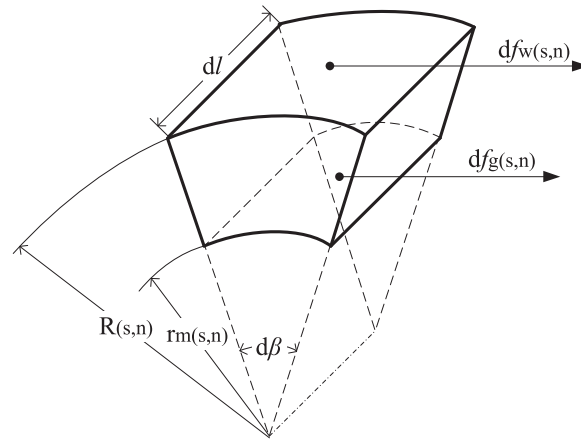


FIG. 2. Control volume in liquid phase.

nozzle, respectively. The friction coefficient for the liquid/gas interface is  $\lambda_{g(v,n)} = 0.3164 Re_{g(v,n)}^{-1/4}$ , where  $Re_{g(v,n)} = 2\rho_g U_\Sigma R_{(v,n)}/\mu_g$ .

Borodin *et al.*<sup>9</sup> evaluated the loss coefficient of angular momentum  $K$  for a swirl injector of which the ratio of the vortex chamber to the inlet diameter is about unity. The result was expressed by an equivalent geometrical characteristic parameter  $A_{eq}$

$$A_{eq} = AK = \frac{R_{in}R_n}{nr_{in}^2 + \frac{\lambda_{in}}{2}R_{in}(R_{in} - R_n)}. \quad (17)$$

Only the friction on the headend wall and in the transition section was taken into account in deriving the above equation. In reality, viscous friction losses on the lateral wall and at the liquid/gas interface in the vortex chamber and discharge nozzle must be considered, and an extended loss coefficient of angular momentum,  $K_e$ , is required to obtain a more accurate characteristic parameter. To this end, we consider a control volume of a swirling annular liquid sheet with a length  $dl$  and a circumferential angle  $d\beta$ , as shown in Fig. 2. The mass of the element in the vortex chamber and discharge nozzle can be obtained as follows:

$$dm_{(v,n)} = 1/2\rho_l(R_{(v,n)}^2 - r_{m(v,n)}^2)d\beta dl. \quad (18)$$

The angular momentum is represented as

$$M'_{(v,n)} = R_{(v,n)}U_{\theta(v,n)w}dm_{(v,n)}. \quad (19)$$

Friction forces on the lateral wall and liquid/gas interface are, respectively,

$$df_{w(v,n)} = \tau_{w(v,n)}R_{(v,n)}U_{\theta(v,n)w}/U_\Sigma d\beta dl, \quad (20)$$

$$\text{where } \tau_{w(v,n)} = \frac{\lambda_{w(v,n)}\rho_l U_\Sigma^2}{4} \frac{\rho_l U_\Sigma^2}{2}$$

$$df_{g(v,n)} = \tau_{g(v,n)}r_{m(v,n)}U_{\theta(v,n)g}/U_\Sigma d\beta dl, \quad (21)$$

$$\text{where } \tau_{g(v,n)} = \frac{\lambda_{g(v,n)}\rho_g U_\Sigma^2}{4} \frac{\rho_g U_\Sigma^2}{2}.$$

The moment of friction force can be expressed as

$$N' = -df_{w(v,n)}R_{(v,n)} - df_{g(v,n)}r_{m(v,n)}. \quad (22)$$

The change of the angular momentum is equal to the moment of external force. Thus,

$$\frac{dM'}{dt} = \frac{dM'}{dl} \frac{dl}{dt} = N'. \quad (23)$$

Noting  $dl/dt = -U_{x(v,n)}$  and substituting the expressions of  $M'$  and  $N'$  to the above equation, we obtain the differential equation determining the change of angular momentum in the swirl injector

$$\frac{\theta_{(v,n)} dM_{(v,n)}}{M_{(v,n)} \sqrt{M_{(v,n)}^2 + \theta_{(v,n)}^2}} = \frac{1}{4} \frac{\lambda_w(v,n) R_{(v,n)} + \alpha \lambda_g(v,n) r_{m(v,n)}}{(R_{(v,n)}^2 - r_{m(v,n)}^2)} dl, \quad (24)$$

where the angular momentum  $M_{(v,n)} = \rho_1 U_{\theta(v,n)w} R_{(v,n)} = \rho_1 U_{\theta(v,n)g} r_{m(v,n)}$  and  $\theta_{(v,n)} = \dot{m} R_{(v,n)} / [2\pi (R_{(v,n)}^2 - r_{m(v,n)}^2)]$ .

Integration of the left hand side of Eq. (23) from  $M_{0(v,n)}$  to  $M_{(v,n)}$  and the right hand side from 0 to  $L_{(v,n)}$  gives

$$\ln \frac{M_{(v,n)}(\theta_{(v,n)} + \sqrt{M_{0(v,n)}^2 + \theta_{(v,n)}^2})}{M_{0(v,n)}(\theta_{(v,n)} + \sqrt{M_{(v,n)}^2 + \theta_{(v,n)}^2})} = \frac{(\rho_1 \lambda_w(v,n) R_{(v,n)} + \rho_g \lambda_g(v,n) r_{m(v,n)}) L_{(v,n)}}{4 \rho_1 (R_{(v,n)}^2 - r_{m(v,n)}^2)}, \quad (25)$$

where  $M_{0(v,n)}$  is the initial momentum in the vortex chamber or the discharge nozzle. The above equation is solved for  $M_{(v,n)}$ ,

$$M_{(v,n)} = \frac{M_{0(v,n)}}{\text{ch} \xi_{(v,n)} + \text{sh} \xi_{(v,n)} \sqrt{\frac{M_{0(v,n)}^2}{\theta_{(v,n)}^2} + 1}}, \quad (26)$$

where  $\xi_{(v,n)} = [(\lambda_w(v,n) R_{(v,n)} + \alpha \lambda_g(v,n) r_{m(v,n)}) L_{(v,n)}] / [4(R_{(v,n)}^2 - r_{m(v,n)}^2)]$ . With the continuity condition  $M_v = M_{0n}$ , the extended angular-momentum loss coefficient,  $K_e$ , can be represented as  $K_e = M_n / M_{0v}$ , where  $M_{0v} = \rho_1 U_{in} R_{in}$ .

In the above derivation, the effect of ambient pressure is introduced into classical theories by taking into account viscous effects at the gas-liquid interface. The model indicates that the viscous loss ( $\xi_v + \xi_n$ ) increases with increasing gas/liquid density ratio, while the angular momentum loss  $e$  decreases with the density ratio. When classical theories<sup>2</sup> are used to determine the velocity and liquid film thickness in the vortex chamber and discharge nozzle, the predicted  $\mu_i$  increases by less than 1% for an ambient pressure increase from 0.10 to 4.83 MPa with a fixed mass flow rate. The experimental data,<sup>7</sup> however, show that  $\mu_i$  increases by up to 4%. This discrepancy suggests that the gas friction loss is probably not a dominant mechanism dictating the ambient pressure effect on the mass-flow coefficient.

## B. Force balance on liquid sheet

The liquid film exits the discharge nozzle and forms a sheet of a conic shape, as shown in Fig. 3. The effect of the ambient pressure on the liquid sheet can be explored by extending the model of Kim *et al.*<sup>6</sup> The analysis is based on the balance of forces on a finite element of an annular sheet originating from the injector exit (see Fig. 3). Gravity is ignored because of its limited influences compared with other forces.

The surface tension force,  $S$ , and the outer static pressure,  $P_{out}$ , tend to cause the liquid sheet to converge. The centrifugal force,  $C$ , and the inner static pressure,  $P_{in}$ , on the other hand, tend to cause the liquid sheet to diverge. The liquid sheet has two principal radii of curvature,  $\xi$  and  $r$ . Decomposition of the surface tension and centrifugal force in the  $\xi$ - and  $r$ -directions gives,  $S_\xi = 2\sigma dS/\xi$  and  $S_r = 2\sigma dS/r$ ,  $C_\xi = \rho_1 (U_x/\cos\varphi)^2 h dS/\xi$ , and  $C_r = \rho_1 U_\theta^2 h dS/r$ , respectively. The force balance at point  $(r, x)$  in the direction normal to the sheet surface can be derived as follows:

$$\frac{2\sigma}{\xi} + \frac{2\sigma}{r} \cos\varphi + \Delta P_d = \frac{\rho_1 (U_x/\cos\varphi)^2 h}{\xi} + \frac{\rho_1 U_\theta^2 h}{r} \cos\varphi, \quad (27)$$

where  $\Delta P_d$  is the pressure difference across the liquid sheet,  $\Delta P_d = P_{out} - P_{in}$ . Equation (27) provides the functional relationship between the radial location of the liquid sheet,  $r(x)$ , and the liquid fluid properties,  $(\sigma, \rho_1)$ , the sheet characteristics,  $(h, U_x, U_\theta)$ , and the pressure difference ( $\Delta P_d$ ). The spreading of the liquid sheet decreases with increasing pressure difference and film thickness. The dominant effects dictating the sheet behavior (in terms of geometry and velocity),

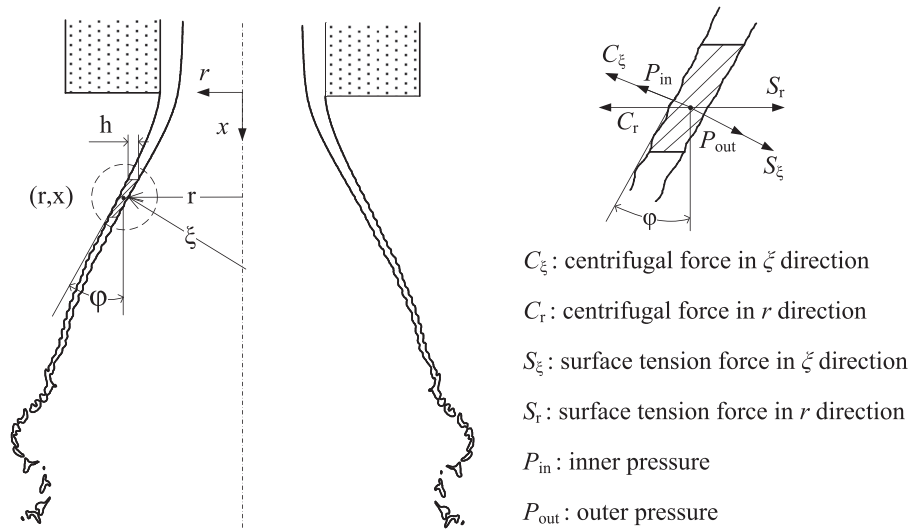


FIG. 3. Force balance on liquid flow element.

however, remain unclear. It is difficult to quantify the impact of individual processes and parameters based on theoretical analyses. Numerical simulations are required to shed light on these questions, especially from a quantitative perspective.

### III. NUMERICAL SIMULATIONS

#### A. Numerical models

The numerical analysis is based on axisymmetric simulations of two-phase flowfields of swirl injectors using commercial software FLUENT 6.3.<sup>10</sup> The formulation includes the full conservation equations for incompressible flows. Turbulence closure is achieved using a Reynolds stress model<sup>10</sup> taking into account anisotropy effects. Non-equilibrium wall functions are employed to improve predictions for flow evolution with pressure gradients. Surface capturing is performed by means of a volume-of-fluid method for arbitrary meshes. The pressure and pressure-velocity coupling terms are treated numerically using a pressure-staggering method and a semi-implicit method for pressure-linked equations, respectively. The momentum equations are discretized by a second-order upwind scheme.

Adaptive mesh refinement is used to substantially improve the numerical accuracy and efficiency for interfacial flow dynamics. The grids near the interface are refined to an extent sufficient to resolve local flow motion. Special attention is given to regions with high turbulent kinetic energy, and to the dissipation rate of the kinetic energy. The maximum level of refinement is controlled to be 2.

#### B. Boundary conditions

Numerical simulations are first made of the swirl injector experiments of Kenny *et al.*<sup>7</sup> for water in an ambient air environment. Table I summarizes the injector geometry, where  $d_{in}$  and  $D_s$  are the diameters of the tangential orifice and vortex chamber, respectively, and  $L_v$ ,  $L_n$ , and  $L_{add}$  the lengths

TABLE I. Geometric parameters of swirl injector.

$d_{in}$ (mm)	$R_{in}$ (mm)	$D_s$ (mm)	$L_v$ (mm)	$D_n$ (mm)	$L_n$ (mm)	$L_{add}$ (mm)	A
1.56	1.55	4.78	3.93	2.08	3.12	14.35	0.88

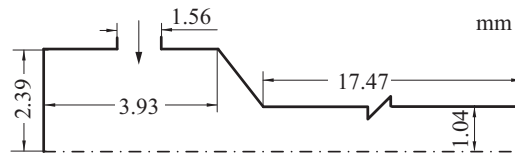


FIG. 4. Geometry of swirl injector.

of the vortex chamber, discharge nozzle, and nozzle extension, respectively. The convergence angle between the swirl chamber and nozzle is  $118^\circ$ .

In the present study, the three circular tangential inlet ports are represented by a slit on the injector wall. The flow variations in the circumferential direction are thus neglected. The analysis nonetheless captures the main features of the injector flow dynamics and helps identify, quantitatively, the key mechanisms.

The computational domain includes the interior of the swirl injector and a downstream region measuring  $10R_n$  and  $10R_n$  in the radial and axial directions, respectively. Figure 4 shows the injector. The tangential entry is set to be at the middle of the vortex chamber. The inlet radial and tangential velocities are calculated based on the mass and angular momentum of the injected liquid. The turbulent intensity is set to be 10%. At the outlet, the static pressure is prescribed. The no-slip condition is enforced along the solid wall. The surface tension of water in air is fixed at 0.07275 N/m. Each simulation was conducted for ten flow-through times to obtain statistically meaningful data.

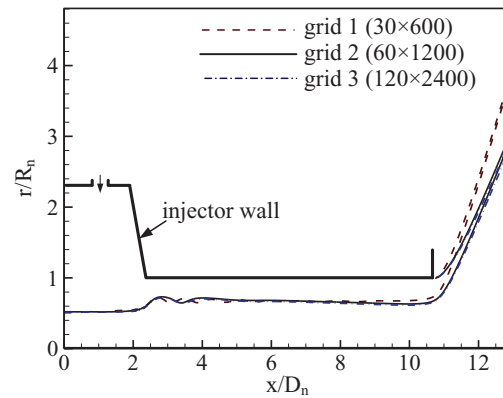
### C. Grid convergence study

Roache<sup>11</sup> suggested a grid convergence index (GCI) based on the use of Richardson's extrapolation to ensure consistent reporting of the results of grid convergence studies and to provide an error band on the grid convergence of solutions. Following the procedure described in Ref. 11, the effect of grid density on calculated flow properties was examined at three different basic levels, each with double the numbers of grid points in the axial and radial directions of the previous level. Adaptive mesh refinement (AMR) is employed on the basic levels. The finest basic grid consists of  $120 \times 2400$  meshes inside the injector. After refinement, the smallest cell size is about  $2 \mu\text{m}$  along the interface.

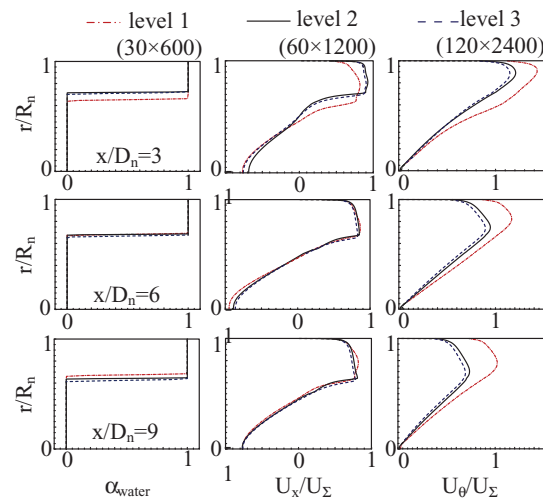
Figure 5(a) shows the interface positions with different grid resolutions. All the calculated interfaces in the nozzle section exhibit a stationary wave pattern, a phenomenon previously observed by Hutt<sup>8</sup> and Kenny *et al.*<sup>7</sup> Figure 5(b) shows the radial distributions of the time-mean liquid volume fraction, and the axial and tangential velocity components at different axial locations. The solution starts to converge at the level 2 resolution. Table II presents the averaged liquid-surface positions from the centerline in the nozzle extension ( $x = 8\text{--}22 \text{ mm}$ ) with three different grid resolutions, where the grid spacing is normalized by the size of the finest grid. The order of convergence calculated following Roache<sup>11</sup> is 2.087, which is close to the theoretical value of 2.0. This suggests that as the grid size decreases, the averaged liquid-surface position approaches an asymptotic value of zero-grid spacing. Applying Richardson's extrapolation, an estimated value of the averaged liquid-surface position at zero grid spacing is calculated to be 0.6926 mm. The GCI for grid levels 1 and 2 is 1.2930% and for grid levels 2 and 3 is 0.3066%. The predicted liquid-surface position falls close to unity, in the asymptotic range of convergence, at 1.0080. Results from the present analysis are well converged. The averaged interface position of grid level 2 has an error band of 1.0396% with respect to the "exact" value. This grid appears to be sufficient to capture the flow dynamics of the swirl injector. After AMR, the grid size on the liquid/gas interface is about  $4 \mu\text{m}$ .

## IV. RESULTS AND DISCUSSION

Following the experiments of Kenny *et al.*,<sup>7</sup> the injector flow dynamics is simulated for ambient pressures in the range of 0.10–4.83 MPa. The mass flow rate of the injector is fixed at 0.09 kg/s.



(a)



(b)

FIG. 5. (a) Liquid-film surface positions with different numerical grids; (b) radial distributions of liquid volume fraction and axial and radial velocity components at different axial locations. ( $P_a = 0.10$  MPa).

### A. Flow dynamics within the injector

The baseline analysis is featured with level-2 resolution. Figure 6 shows the time-mean distribution of the liquid-surface position along the nozzle. Four different flow regimes exist within the injector. In the developing regime close to the injector headend, the liquid enters the vortex chamber tangentially and forms a thick film. The small axial velocity causes the injected liquid to spread over a substantial fraction of the injector volume. When the film reaches the transition step of the injector, an accelerating regime emerges, in which the decreased cross sectional area forces the axial velocity to increase due to the conservation of mass. This leads to a decrease of the tangential velocity. The

TABLE II. Grid information and averaged liquid-surface position in the nozzle.

Grid level	Normalized grid spacing	Liquid-surface position (mm)
1 (30 × 600)	4	0.7234
2 (60 × 1200)	2	0.6998
3 (120 × 2400)	1	0.6942

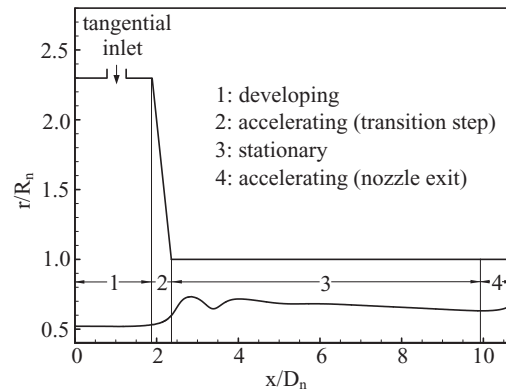


FIG. 6. Evolution of liquid film along injector wall ( $P_a = 0.10$  MPa).

interface position accordingly moves toward the wall. In the stationary regime downstream of the transition step, the radial distributions of the flow properties vary slowly along the axial direction.<sup>4</sup> Interestingly, a stationary wave appears in the nozzle extension. Excluding the effect of the stationary wave, viscous friction causes the film thickness to increase along the wall.<sup>4</sup> Finally, as the static pressure induced by the swirling motion is converted into axial acceleration close to the injector exit,<sup>12</sup> the axial velocity increases and the film thickness decreases.

Figure 7 shows the radial distributions of the time-mean flow properties at various axial locations in the nozzle section. The liquid-surface position is marked with black dots. Sharp transitions of the flow properties on the interface are well resolved. The profiles bear close similarity except at  $x/D_n = 4$ , where the distributions are affected by the stationary wave. As shown in Fig. 7(a), the liquid film behaves like a turbulent boundary layer on the wall. The axial velocity decreases along the nozzle, due to viscous friction. Consequently, the liquid film thickness increases in the downstream region to maintain the mass continuity. The axial velocity in the gas phase at the centerline is opposite to the direction of the liquid phase, and has a value approximately equal to that at the interface. Figure 7(b) shows that the tangential velocity in the gas phase increases linearly with radius. On the other hand, the velocity in the liquid film decreases radially and reaches zero at the wall. Note that the present axisymmetric model does not consider the swirl decay, and the centrifugal momentum remains conservative along the axis. The decrease of the tangential velocity along the nozzle is mainly caused by the increasing film thickness. The radial velocity (not shown) is smaller than 1% of the total velocity. The assumption of zero radial velocity in classical theory is thus corroborated. Figure 7(c) shows that the static pressure in the liquid film increases radially and decreases axially, a phenomenon associated with the variations of the tangential velocity.<sup>12</sup> On the other hand, the static pressure in the gas phase increases axially.

The flowfield in the injector can be divided into four different regimes radially, as shown in Fig. 8. In the wall region, the tangential velocity reaches zero rapidly to form a wall boundary layer. A free vortex is observed near the wall, where the angular momentum,  $U_\theta r$ , remains constant. The tangential velocity is given by  $U_\theta = \Gamma/2\pi r$ , where  $\Gamma$  is the constant circulation and  $r$  the radial distance from the centerline.<sup>13</sup> On the other hand, in the forced vortex regime in the gas phase, the angular velocity,  $\omega$ , remains constant, with the tangential velocity being  $U_\theta = \omega r$ . The angular momentum thus increases with the radial position. In the transition regime formed by the tangential shear stress on the interface, the tangential velocity profile varies smoothly between the forced vortex and free vortex regimes. Figure 8 also shows the axial velocity distribution at the same axial location. It follows the same trend as its tangential velocity counterpart. The transition regime, however, cannot be clearly distinguished from the free vortex regime, mainly because of the small shear stress in the gas phase. As will be further discussed in Sec. IV B, when the density of the gas phase is high, the shear stress in the gas phase can affect the axial velocity profile to alter the distribution in the transition regime.

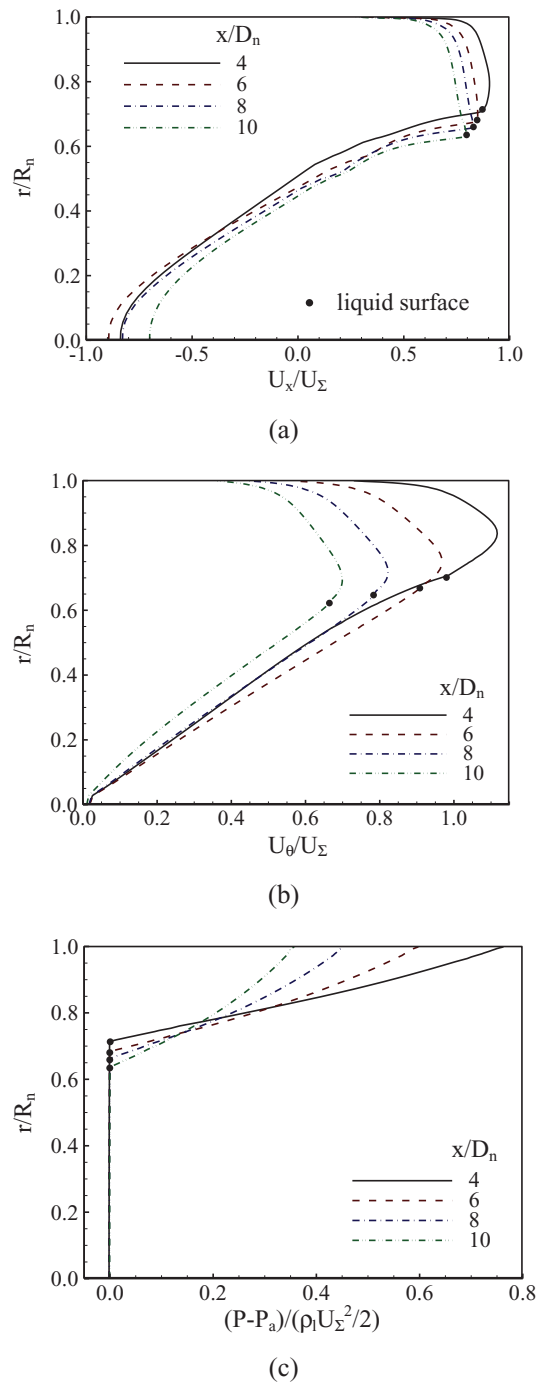


FIG. 7. Radial distributions of time-mean flow properties at different axial positions ( $P_a = 0.10$  MPa). (a) Axial velocity; (b) tangential velocity; (c) static pressure.

## B. Effect of ambient pressure on film thickness

Since turbulence information is not available from experiments,<sup>7</sup> a parametric study was conducted to explore the effect of turbulent intensity  $I_t$  on the flow evolution. Figure 9 shows the calculated interface positions for a range of  $I_t = 10\%$ -40% at the inlet. Stationary waves are clearly observed in the nozzle section in all the cases considered here. The liquid film becomes thicker for

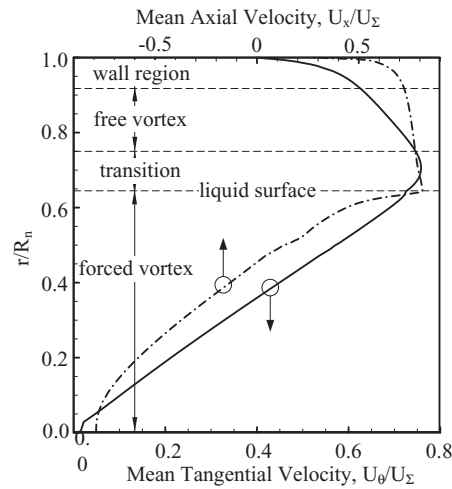


FIG. 8. Flow regimes in swirl injector,  $x/D_n = 9$  ( $P_a = 0.10$  MPa).

a higher  $I_t$  due to the increased turbulent viscosity. The maximum liquid film thickness increases by 25.6% when  $I_t$  increases from 10% to 40%.

The effect of ambient pressure on the injector flow dynamics is examined for five different ambient pressures of 0.10, 1.38, 2.76, 3.79, and 4.83 MPa. The inlet turbulent intensity is fixed at 30% to obtain the best match with measured film thickness. Figure 10(a) shows the calculated interface positions inside the nozzle. The film thickness increases with increasing pressure. Figure 10(b) shows a comparison of the time-mean film thickness near the nozzle exit with experimental data, normalized by the value for 0.1 MPa. The discrepancy may arise from the neglect of the tangential shear stress in the present axisymmetric model, which weakens the effect of gas density on the film thickness.

Figure 11 shows the radial distributions of time-mean velocity components at  $x/D_n = 9$ . The velocity in the liquid film remains almost the same in the five cases, except in the transition regime, where the velocity varies more gradually with increasing ambient pressure.

The shear stress in the axial direction at the interface can be expressed as  $\tau_g = -\mu \partial U_x / \partial r + \rho_g \tau_a$ , where  $\tau_a$  is the axial Reynolds stress. Figure 12 shows the results for different ambient pressures. The absolute shear stress increases with the ambient pressure. The ensuing reduction of the axial velocity leads to an increased film thickness, to satisfy the mass continuity. The axial velocity profile in the gas phase inside the injector is similar to the boundary flow over a flat plate, and can be approximated by a second-order polynomial varying from 0 to  $2U_{xn}$  with respect to the interface. The mean axial velocity is then calculated to be  $4/3U_{xn}$ .

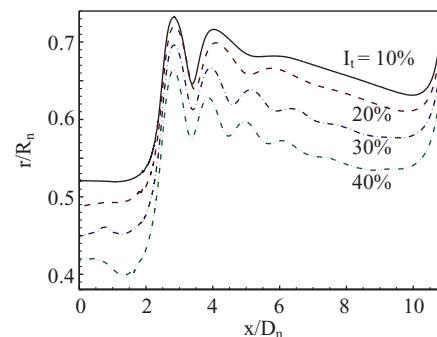


FIG. 9. Effect of inlet turbulence intensity on liquid-film surface evolution ( $P_a = 0.10$  MPa).

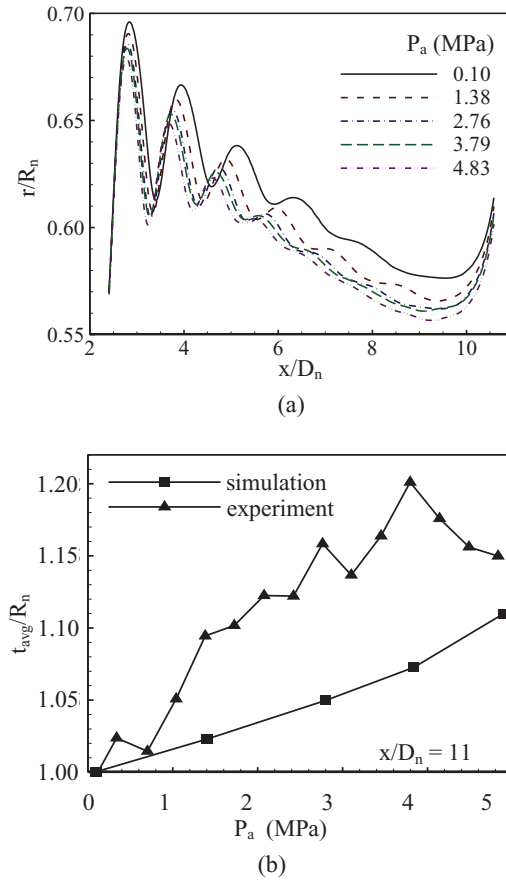


FIG. 10. (a) Effect of ambient pressure on liquid-film surface evolution; (b) measured and calculated liquid surface locations at different ambient pressures ( $x/D_n = 11$ , immediately upstream of nozzle exit).

Using the expression of the shear stress on the wall for fully developed turbulence,<sup>14</sup> the shear stress on interface can be derived to be

$$\tau_g = -0.05057\rho_g U_{xn}^2 \text{Re}_g^{-1/4}, \quad (28)$$

where  $\text{Re}_g = \rho_g U_{xn} h / \mu_g$  with  $h$  being the liquid film thickness. If  $U_{xn}$  and  $h$  take the values at 0.10 MPa for simplification, Eq. (28) shows that shear stress on the interface is a quasilinear function of air density. As shown in Fig. 12, this equation underestimates the actual value. One factor contributing to this phenomenon is the neglect of the centrifugal force in the empirical expression for the gas-phase velocity profile. A much-improved comparison is obtained with the numerical simulation if the coefficient in Eq. (28) is multiplied by a factor of 4 as follows:

$$\tau_g = -0.20228\rho_g U_{xn}^2 \text{Re}_g^{-1/4}. \quad (29)$$

If the flow variation in the transition regime is ignored, the axial velocity in the liquid film can be described by the one-seventh power profile. Following the approach of Inamura,<sup>15</sup> the effect of shear stress at the interface can be included in the following expression for the film thickness normalized by the theoretical film thickness:

$$h^* = 0.02893 \left( \frac{x^*}{\text{Re}_1^{1/4}} \right) + 0.2601 \frac{\rho_g}{\rho_l} \left( \frac{x^*}{\text{Re}_g^{1/4}} \right) + C_1. \quad (30)$$

The above equation gives an increase in the film thickness of only about 3.2% when ambient pressure increases from 0.10 to 4.83 MPa. This is considerably lower than the experimental and simulation

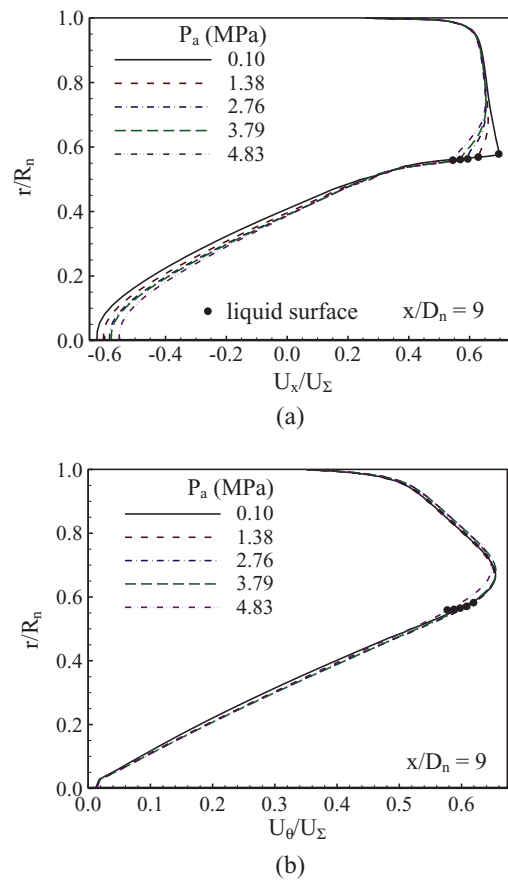


FIG. 11. Radial distributions of mean velocity components at different ambient pressures ( $x/D_n = 9$ ). (a) Axial velocity; (b) tangential velocity.

data shown in Fig. 10(b), and indicates that the change of the axial velocity profile by the shear stress at the interface is significant and most likely the reason for the large variation in the film thickness.

When the liquid film is discharged into the ambient environment from the nozzle exit, the static pressure in the liquid film decreases rapidly to the ambient value. The process leads to acceleration of the liquid film and a decrease in the film thickness. Experimental results<sup>7</sup> have shown that although the film thickness inside the nozzle increases by about 15% for an ambient pressure increase from

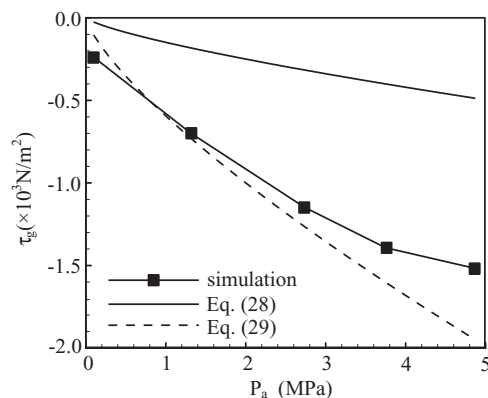


FIG. 12. Effect of pressure on spatially averaged shear stress at liquid-film surface in nozzle section.

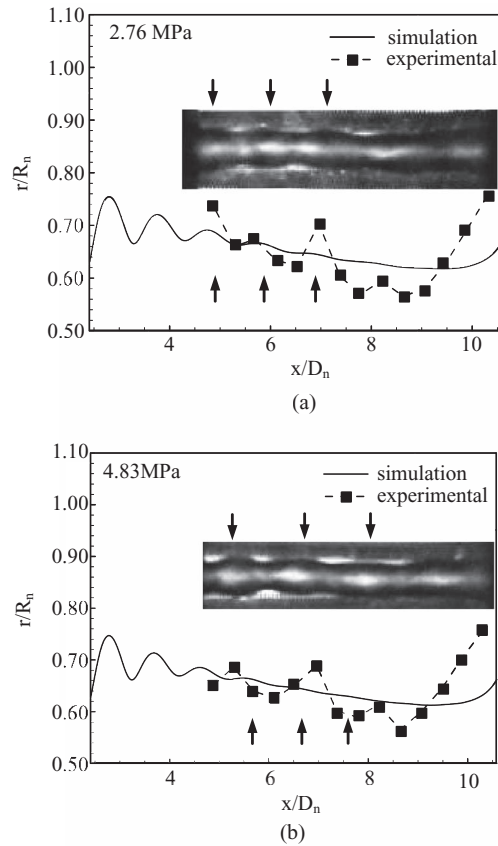


FIG. 13. Calculated and measured liquid surface evolution for different ambient pressures: (a) 2.76 MPa; (b) 4.83 MPa.

0.10 to 4.83 MPa, the liquid film at the nozzle exit increases by only about 3.0%. This observation shows good agreement with the increase of 2.5% obtained from the numerical simulation.

### C. Stationary wave in the nozzle

The existence of stationary waves in the nozzle of a swirl injector was noticed by several researchers.<sup>7,8</sup> No investigation of the underlying physics, however, was conducted. The present study shows that stationary waves appear under all the operating conditions considered. The wave form is time-invariant, except for those small fluctuations caused by turbulence. The wave crests remain at the same location in spite of the convection of the mean flow. A detailed analysis of the physics of a stationary gravity wave can be found in Ref. 16. The occurrence of a stationary wave is attributed to the dispersive property of waves. That is, the wave speed varies with the wavelength, and possibly also with the direction of propagation. This allows some waves to propagate in the direction opposite to the fluid motion. If the value of the wave speed is equal to that of the flow velocity, the wave can be stationary. The group velocity, which represents the velocity of energy propagation, cannot be larger than the wave speed. The energy in stationary waves is therefore always swept downstream. The energy in a long wave normally attenuates rather slowly and may be present even at a considerable distance behind the obstacle.<sup>16</sup>

Figure 13 compares the numerical and measured<sup>7</sup> interface positions for 2.76 and 4.83 MPa. The underestimation of the wave amplitude by the numerical simulation can be attributed to the approximation of the three injection orifices by a circumferential slit. The neglect of flow nonuniformity in the azimuthal direction eliminates the helical pattern of the liquid film, thereby modifying the wave characteristics. The arrows in Fig. 13 indicate the locations of the wave troughs in both the experimental images and simulation results. Reasonable agreement is achieved.

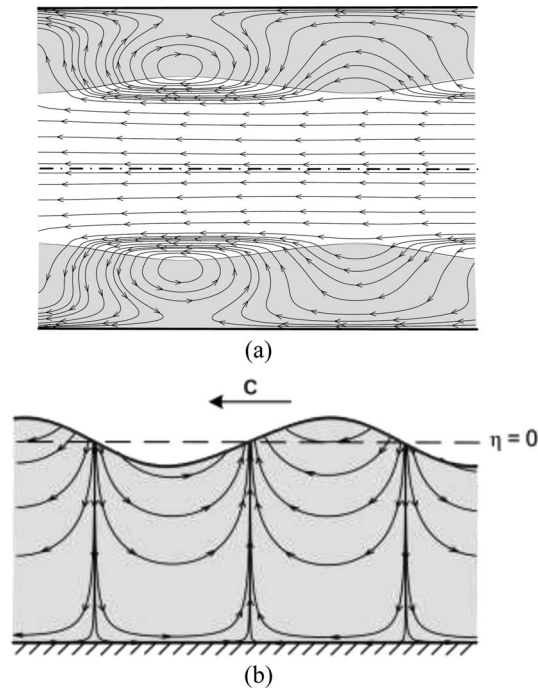


FIG. 14. Instantaneous streamlines in a stationary wave. (a) Swirl injector nozzle; (b) shallow water.

In classical hydrodynamics theory, the dynamics of the liquid film inside the vortex chamber and nozzle are modeled by means of a wave equation taking into account the disturbance propagation in the liquid with the centrifugal force. The surface-wave propagation speed  $U_w$  is<sup>2</sup>

$$U_w = \sqrt{\left(\frac{U_{in}^2 R_{in}^2}{r_{mn}^3}\right) \left(\frac{R_n^2 - r_{mn}^2}{2r_{mn}}\right)} = \frac{U_{in} R_{in}}{r_{mn}^2} \sqrt{\frac{R_n^2 - r_{mn}^2}{2}}. \quad (31)$$

The first parenthesized term in the square root represents centrifugal acceleration, while the second represents the effective thickness of the liquid layer. The situation is analogous to that of shallow-water wave propagation. In the present study, it is the centrifugal force that attaches the liquid to the wall, and the interfacial wave of the swirling liquid is called a “centrifugal surface wave.”

The flow development in the nozzle follows the principle of maximum flow.<sup>17</sup> Applying  $\partial r_{mn}/\partial x = 0$  to the continuity equation of the liquid phase in the nozzle, the axial velocity in the nozzle is expressed as<sup>17</sup>

$$U_{xn} = \frac{U_{in} R_{in}}{r_{mn}^2} \sqrt{\frac{R_n^2 - r_{mn}^2}{2}}. \quad (32)$$

The axial velocity in the nozzle becomes identical to the surface wave speed. If the liquid-film thickness and radial velocity are ignored, the solution to the wave equation characterizing the flow oscillation in the nozzle becomes<sup>2</sup>

$$\xi_f = \Omega e^{i\omega(t-x/U_w)}. \quad (33)$$

Note that Eq. (33) does not consider the movement of the liquid. The coordinate is changed to  $x+U_{xn}t$  for the moving fluid,

$$\xi_f = \Omega e^{i\omega[(1-U_{xn}/U_w)t-x/U_w]}. \quad (34)$$

This equation shows that the wave pattern is stationary if and only if  $U_w = U_{xn}$  and the wave direction is inverse to that of the liquid flow. Figure 14(a) shows the instantaneous streamlines in the liquid film, with the coordinate system travelling with the mean axial velocity of the liquid film.

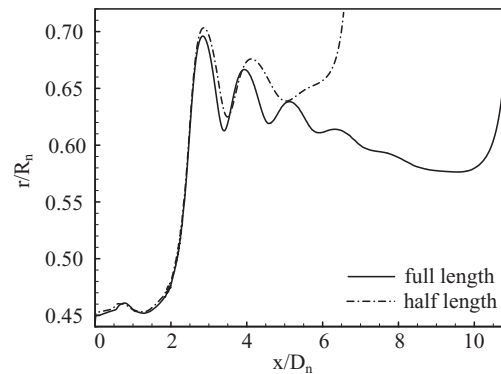


FIG. 15. Normalized liquid-surface positions with two different nozzle lengths ( $P_a = 0.10$  MPa).

For comparison, a gravity wave in shallow water is shown in Fig. 14(b). For the gravity wave, the flow velocity is in the direction of wave propagation underneath the crests, but becomes opposite below troughs.<sup>18</sup> In a swirl injector, the wave propagates from the nozzle to the vortex chamber with a phase speed equal to the mean axial speed. A stationary wave thus takes place in both time and space.

The effect of the nozzle length on the wave behavior is also explored. Figure 15 compares the interface position for two different nozzle lengths. The wave amplitude in the transition section appears to be insensitive to the nozzle length. The wave is generated in the transition section and decays as the flow is convected downstream.

The characteristics of the stationary wave in a swirl injector are similar to those discussed by Lighthill<sup>16</sup> and Lord Rayleigh.<sup>19</sup> They showed theoretically that two stationary waves can be generated by a standing disturbance or an obstacle to the flow. As illustrated in Fig. 16, the wave upstream of the obstacle is a capillary wave with a short wavelength, while the wave in the downstream region is a gravity wave with a long wavelength. The stationary capillary wave also takes place in the present study, with the transition section acting as the obstacle. The stationary capillary wave in the injector has, however, an extremely small wavelength, comparable to the grid size, and is thus not accurately resolved.

#### D. Effect of ambient pressure on liquid sheet

Figure 17 compares the measured<sup>7</sup> and calculated liquid sheet issuing from the injector nozzle. Good agreement is achieved for the case of 4.83 MPa, and the difference for 0.10 MPa is obvious. The liquid sheet is curved with respect to the centerline at a high pressure condition and changes from a conic shape to a contracting bell at the breakup point.

Figure 18(a) shows the time-mean streamlines near the nozzle exit. The interfaces are represented by thick lines. A recirculation zone forms in the gas-phase region surrounded by the liquid sheet. The ambient gas flows into the injector in the center region and then moves out along the liquid sheet. The size of the recirculation zone decreases with increasing ambient pressure. Figure 18(b) shows the distribution of the gauge pressure in reference to the ambient pressure under four different

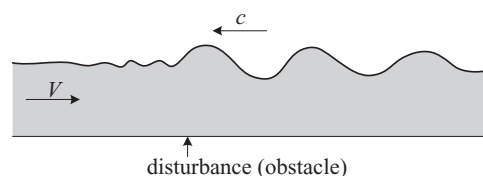


FIG. 16. Schematic of generation of stationary wave by a disturbance (obstacle).

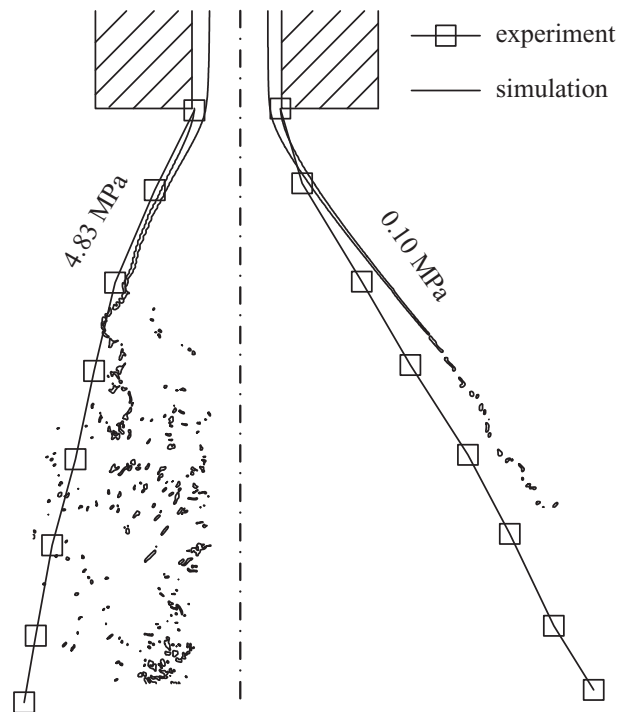


FIG. 17. Measured and calculated evolution of liquid sheet at two different ambient pressures ( $P_a = 0.10$  and  $4.83$  MPa).

ambient conditions. The pressure reduction across the liquid sheet increases with increasing ambient pressure.

Figure 19 shows the time-mean pressure differences between the inner and outer interfaces of the liquid sheet. Values are maximum at the nozzle exit, decrease rapidly due to the flow adjustment, and then smooth out at the breakup point. The maximum pressure difference is on the same order as that reported in Ref. 5. The result, combined with Eq. (27), clearly indicates that a higher ambient pressure tends to confine the spread of the liquid sheet.

As shown in Figs. 18 and 19, the breakup length of the liquid sheet decreases when the ambient pressure is changed from  $0.10$  to  $1.62$  MPa, but increases as the pressure is increased from  $1.62$  to  $4.83$  MPa. The decrease of the breakup length with ambient pressure was observed by Kim *et al.*<sup>6</sup> and is attributed to increased aerodynamic drag. Considering different flow parameters, the present study observes suppressed liquid sheets at higher ambient pressure. The shifting of the radial position of the sheet for a given axial position leads to increased thickness, due to the conservation of mass. The thick liquid sheet should break up over a longer distance; breakup length increases with higher ambient pressure.

Figure 20(a) shows the radial distribution of the time-mean axial velocity at four different axial locations outside the nozzle exit. The maximum velocity occurs at the liquid sheet. Although the peak location changes along the radial direction, the peak value varies little with the axial location for different pressures. This means that the axial velocity of the liquid sheet can be considered constant. The velocity near the outer interface of liquid sheet decreases rapidly to zero, while the gas velocity inside the liquid cone varies more smoothly. Figure 20(b) shows the radial distribution of the time-mean tangential velocity. At the location close to the nozzle exit, the curves are almost identical for different ambient pressures. The tangential velocity of the gas phase is almost zero outside the liquid sheet; inside the liquid sheet it increases from zero to that of the liquid sheet. For each ambient pressure, it decreases with increasing radial location, and angular momentum is conserved.

Following the Bernoulli theorem, the static pressure in the gas phase can be expressed as  $P_s = P_t - 1/2\rho_g U_t^2$ , where  $P_s$  is the static pressure,  $P_t$  the total pressure,  $\rho_g$  the gas density, and  $U_t$

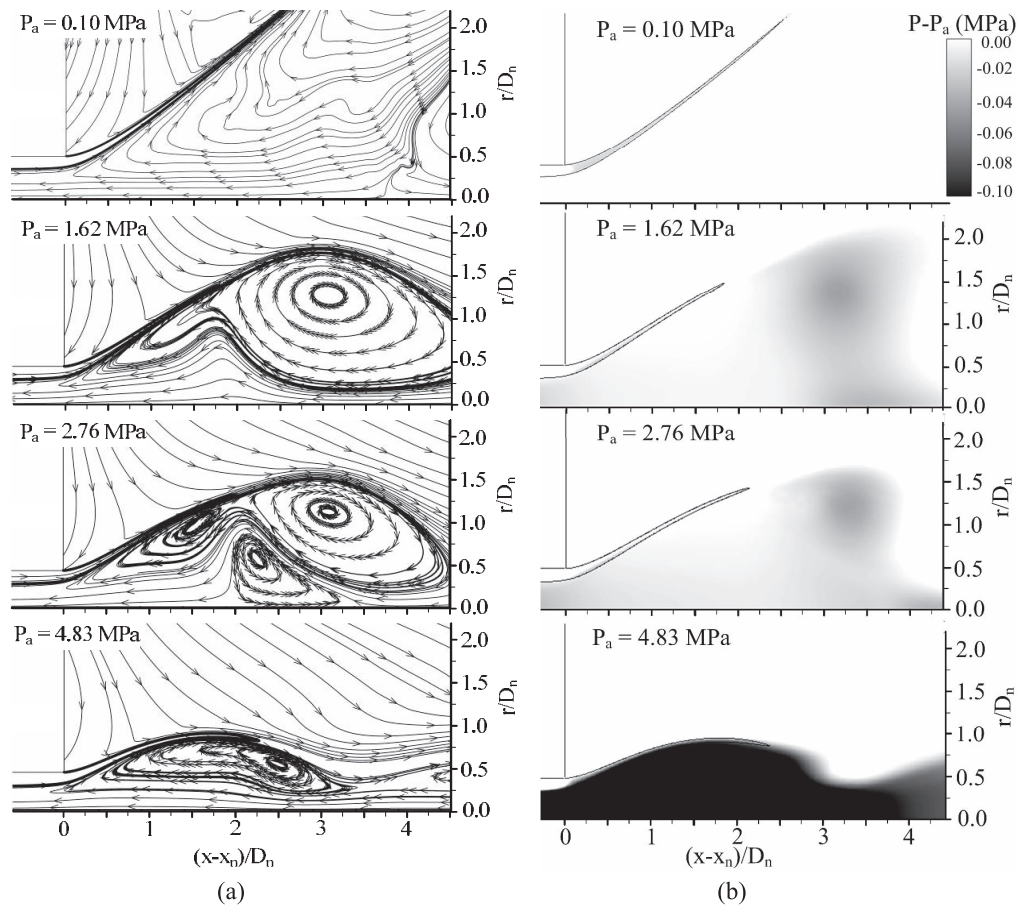


FIG. 18. (a) Streamlines downstream of nozzle exit at different ambient pressures; (b) time-mean distributions of gauge pressure at different ambient pressures.

the total velocity of the gas phase. From the observation of velocity distributions in Fig. 20, the gas outside the liquid sheet can be considered stagnant and the pressure is equal to the total pressure. The pressure difference across the liquid sheet can then be expressed as  $\Delta P_d = 1/2 \rho_g U_t^2$ , which is linearly proportional to the gas density. Based on the results shown in Fig. 20, the axial and tangential velocities of the gas phase at the inner interface of the liquid sheet are approximately 2/5

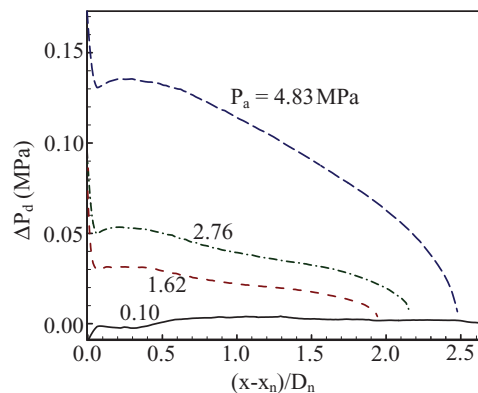


FIG. 19. Effect of ambient pressure on pressure difference across liquid sheet downstream of nozzle exit.

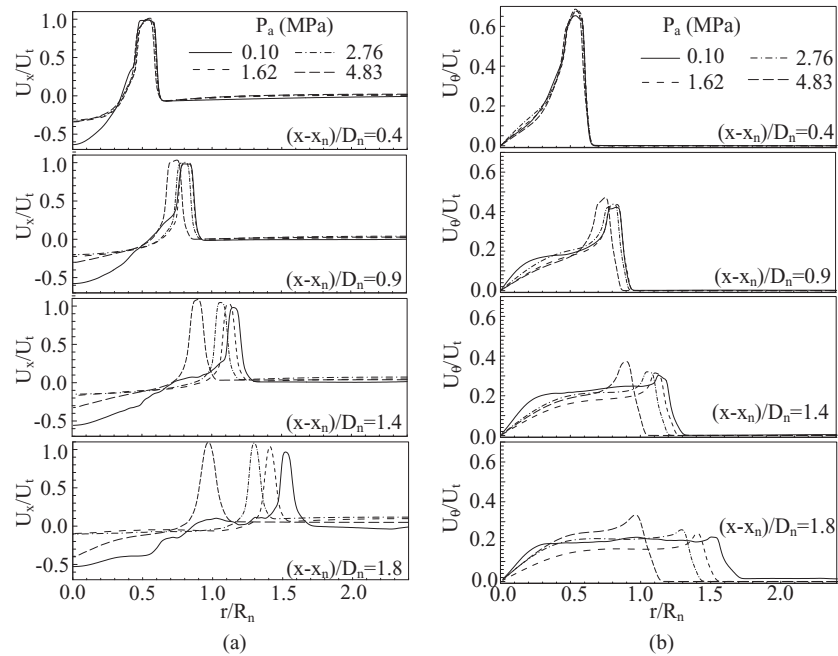


FIG. 20. Radial distributions of time-mean velocity components at different downstream locations. (a) Axial velocity; (b) tangential velocity.

and  $4/5$  of the velocity of the liquid sheet. A semi-empirical model can thus be established by using  $1/2\rho_g[(2/5U_x)^2 + (4/5U_\theta)^2]$  to express the pressure difference across the liquid sheet.

With the definition of the radius of curvature, Eq. (27) can be solved as an ordinary differential equation for the spatial distribution of the liquid sheet. The flow parameters of the liquid film at the nozzle exit are obtained from the simulation result for 0.10 MPa. Figure 21 shows the calculated shapes of the liquid sheet for different ambient pressures. Note that the predicted curves terminate at the points where the slope reaches infinity. Since no breakup mechanism is applied in the model, breakup length could not be predicted here. Figure 22 compares the theoretical and experimental results of two limit cases. The shapes of the liquid sheet for the two pressures are well predicted. Figure 23 shows good agreement of the calculated liquid spreading angle at the nozzle exit with experimental data.<sup>7</sup> It is worth noting that Kim *et al.*<sup>6</sup> in their experiment indicated that the ambient

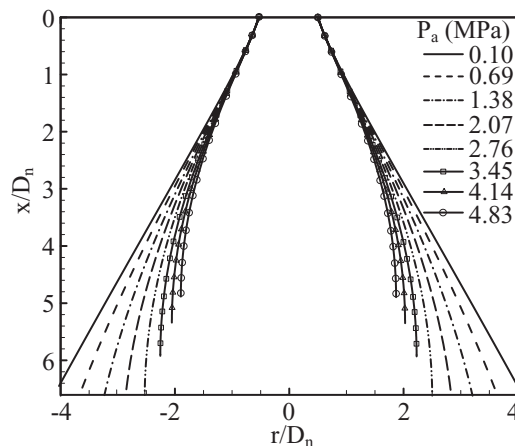


FIG. 21. Liquid sheet distributions at different ambient pressures.

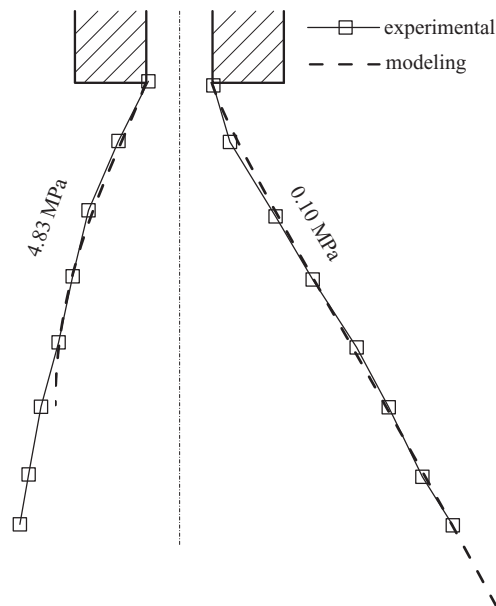


FIG. 22. Measured and predicted liquid sheet distributions at two different ambient pressures.

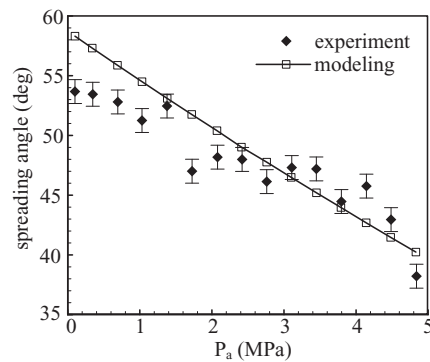


FIG. 23. Measured and calculated spread angles of liquid sheet at different ambient pressures.

pressure has negligible effect on the spreading angle before breakup. The discrepancy may arise from differences in flow parameters. The exit velocities from Ref. 6 are about half of that in Ref. 7. The smaller pressure difference associated with the lower exit velocity may not be sufficient to change the shape of the liquid sheet before it disintegrates.

## V. CONCLUSION

The effect of the ambient pressure on the flow dynamics of a liquid swirl injector has been investigated by means of a combined theoretical and numerical analysis. Both the internal and external flowfields were examined in detail. The liquid film thickness was found to increase with increasing pressure. A major factor contributing to this phenomenon is the modification of the velocity distribution near the interface in the liquid film due to the alternation of the interfacial shear stress with pressure. The generation and existence of a stationary wave in the injector nozzle was explored. The underlying physical mechanisms were identified. At a higher pressure, the pressure drop across the liquid sheet downstream of the nozzle exit increases, thereby suppressing the liquid expansion in the radial direction and decreasing the spreading angle. Despite the common wisdom that the breakup length of the liquid sheet decreases with increasing gas density, owing to

aerodynamic drag, the inward offset of the liquid sheet at higher pressure causes the thickness of the liquid sheet to increase, thereby increasing the breakup length. A semi-empirical model was established to predict the shape of the liquid sheet. Good agreement was achieved with experimental observations.

## ACKNOWLEDGMENTS

This work was sponsored partly by the (U.S.) Air Force Office of Scientific Research (USAFOSR) under Grant No. FA-9550-10-1-0179, and partly by the William R. T. Oakes Endowment of the Georgia Institute of Technology. The authors gratefully acknowledge support and encouragement from Dr. Mitat A. Birkan.

- <sup>1</sup> V. G. Bazarov and V. Yang, "Liquid-propellant rocket engine injector dynamics," *J. Propul. Power* **14**, 797 (1998).
- <sup>2</sup> V. G. Bazarov, V. Yang, and P. Puri, "Design and dynamics of jet and swirl injectors," in *Liquid Rocket Thrust Chambers: Aspects of Modeling, Analysis, and Design*, Progress in Astronautics and Aeronautics Vol. 200, edited by V. Yang, M. Habiballah, J. Hulka, and M. Popp (AIAA, 2004), Chap. 2, p. 19.
- <sup>3</sup> Y. Huang and V. Yang, "Dynamics and stability of lean-premixed swirl-stabilized combustion," *Prog. Energy Combust. Sci.* **35**, 293 (2009).
- <sup>4</sup> N. Zong and V. Yang, "Cryogenic fluid dynamics of pressure swirl injectors at supercritical conditions," *Phys. Fluids* **20**, 056103 (2008).
- <sup>5</sup> S. M. De Corso and G. A. Kemeny, "Effect of ambient and fuel pressure on nozzle spray angle," *Trans. ASME* **79**, 607 (1957).
- <sup>6</sup> D. Kim, J. Im, H. Koh, and Y. Yoon, "Effects of ambient gas density on spray characteristics of swirling liquid sheets," *J. Propul. Power* **23**, 603 (2007).
- <sup>7</sup> R. J. Kenny, J. R. Hulka, M. D. Moser, and N. O. Rhys, "Effect of chamber backpressure on swirl injector fluid mechanics," *J. Propul. Power* **25**, 902 (2009).
- <sup>8</sup> J. J. Hutt, "A study of design details of rocket engine swirl injection elements," Ph.D. thesis, Pennsylvania State University, University Park, PA, 2000.
- <sup>9</sup> V. A. Borodin, Y. F. Dityakin, L. A. Klyachko, and V. I. Yagodkin, *Atomization of Liquids (edited machine translation)* (Foreign Technology Division, Dayton, OH, 1968).
- <sup>10</sup> Fluent 6.3 User's Guide (Fluent Inc., Lebanon, NH, 2006).
- <sup>11</sup> P. J. Roache, *Verification and Validation in Computational Science and Engineering* (Hermosa Publishers, Albuquerque, NM, 1998).
- <sup>12</sup> L. Bayvel and Z. Orzechowski, *Liquid Atomization* (Taylor & Francis, Washington, DC, 1993), pp. 252–261.
- <sup>13</sup> F. Chang and V. K. Dhir, "Turbulent flow field in tangentially injected swirl flows in tubes," *Int. J. Heat Fluid Flow* **15**, 346 (1994).
- <sup>14</sup> R. Fox and A. Mc Donald, *Introduction to Fluid Mechanics* (John Wiley and Sons, Inc., New York, NY, 1985).
- <sup>15</sup> T. Inamura, "Characteristics of liquid film and spray injected from swirl coaxial injector," *J. Propul. Power* **19**, 632 (2003).
- <sup>16</sup> J. Lighthill, "Wave patterns made by obstacles in a steady stream," *Waves in Fluids* (Cambridge University Press, Cambridge, 2002), p. 260.
- <sup>17</sup> J. J. Chinn, "An appraisal of swirl atomizer inviscid flow analysis, Part 1: The principle of maximum flow for a swirl atomizer and its use in the exposition and comparison of early flow analyses," *Atom. Sprays* **19**, 263 (2009).
- <sup>18</sup> P. K. Kundu and I. M. Cohen, *Fluid Mechanics* (Academic Press, 2004).
- <sup>19</sup> Lord Rayleigh, "The form of standing waves on the surface of running water," *Proc. London Math. Soc.* **XV**, 69 (1883).